# SUPPORTING INFORMATION

## Bioderived and all-solution-processed tribolayer component enables adaptive design of flexible nanocellulosic triboelectric nanogenerators

Bushara Fatma,*[a,d] Ioannis Ziogas,[b] Rishow Kumar,[c] Rami A. Elkaffas,[d] Ashish Garg[e], Yarjan A. Samad,[d] Leontios Hadjileontiadis,[b,h] Blaise L. Tardy,[f] Charalampos Pitsalidis*[a,g]

[a.] Department of Physics, Khalifa University, Abu Dhabi, 127788, UAE
[b.] Department of Biomedical Engineering, Khalifa University, Abu Dhabi, 127788, UAE
[c.] Department of Materials Science and Engineering, Indian Institute of Technology Kanpur, 208016, UP, India
[d.] Department of Aerospace Engineering, Khalifa University, Abu Dhabi, 127788, UAE
[e.] Department of Sustainable Energy Engineering, Indian Institute of Technology Kanpur, 208016, UP, India
[f.] Department of Chemical & Petroleum Engineering, Khalifa University, Abu Dhabi, 127788, UAE
[g.] Advanced Research and Innovation Center (ARIC), Khalifa University of Science and Technology, Abu Dhabi, UAE
[h.] Department of Electrical and Computer Engineering, Aristotle University of Thessaloniki, GR 54124 Thessaloniki, Greece

Corresponding authors: Charalampos.pitsalidis@ku.ac.ae , Bushara.fatma@ku.ac.ae

## *1. Preparation of different types of nanocellulose (NC)*

### *1.1. Never-dried cellulose nanocrystal (NDCNC)*

Never-dried cellulose nanocrystals (CAS No. 7789-20-0) were produced by dissolving wood fibers using 64 wt% sulfuric acid hydrolysis for an hour at 45°C, followed by dilution with reverse osmosis and bleaching with sodium chlorite. It was further neutralized using sodium hydroxide and obtained as a thick slurry (10 wt%) after membrane filtration. These NDCNCs with typical dimensions of 5–20 nm in width and 150–200 nm in length and sulfur content of 0.95 wt% were produced in the form of suspension in water by USDA's Forest Products Laboratory (FPL, Madison, WI) and acquired through the Process Development Center (University of Maine, USA). A thorough characterization of the NDCNC suspension used in this study was previously performed.[1, 2] Millipore (Synergy UV) milli-Q water was used to dilute the CNC suspension to a desirable concentration before use.

### *1.2. Cellulose nanofibril (CNF)*

CNF were prepared using a microfluidization of never-dried, fully bleached sulfite birch pulp (Kappa number of 1 and DP of 4700) after washing it with 0.01 M HCl to filter the residual metal ions and then with deionized (DI) water until the pH reached 5. The washed fiber suspension in DI water with a mass fraction of 1.8% (w/v) was disintegrated by passing it through a high-pressure fluidizer (Microfluidics M110P, Microfluidics Int. Co., Newton, MA). A homogeneous and thick gel-like suspension was obtained after the 9th pass. The CNF used herein has been previously reported and characterized in depth.[3, 4]

### *1.3. Spray-dried cellulose nanocrystal (SDCNC)*

Spray-dried cellulose nanocrystals (SDCNCs) used in these examples were produced at an industrial scale by CelluForce (Montreal, Quebec). The largest producer of sulfuric acid (64 wt%) hydrolyzed cellulose nanocrystals (CNC) produced from breached Kraft pulp.[5] After hydrolysis, the product was neutralized to its sodium form and spray-dried.

### *1.4. Tempo-oxidized cellulose nanofibril (TOCNF)*

Tempo-oxidized cellulose nanofibrils were produced by carboxylation of bleached birch fibers with alkaline 2,2,6,6,-tetramethylpipelidine-1-oxyl radical (TEMPO)-NaBr-NaClO, following the process reported previously.[6] Initially, the fibers (45 g) were treated with 0.9 g of TEMPO and 21.6 g of NaBr in 4.5 L of DI water while maintaining the pH at 10 using NaOH, followed by the addition of 13.4 g of NaOCl. During the oxidation process, the pH of the solution was maintained at a constant level for 1.5 hours. The obtained product was washed three times with 2.5 pH water using Buchner filtration, followed by three washes with deionized (DI) water. The synthesis and properties of tempo-oxidized cellulose nanofibril (TOCNF) have been reported before.[3, 4, 7]

## *2. Preparation of graphene ink*

Commercial graphite with particle sizes less than 100 microns was suspended in water along with the surfactant (Sodium Dodecyl Sulfate). The final suspension was homogenized using a high-pressure homogenizer (PSI-30), with an applied pressure exceeding 500 bars. The shear-induced graphene was produced in the microfluidic channel by exfoliating graphite. For the preparation of a few-layer graphene suspension, the process was repeated for ~100 cycles. The final product was centrifuged at 10000 rpm for 30 minutes to separate the stable few-layer graphene suspended in water. The concentration of the few-layer graphene suspension was estimated to be ~10 g/l, which was further used for spray coating.

### *3. Preparation of castor oil-based film (tribonegative layer)*

Fabrication of castor oil (CO) film is reported in our recently published work where the detailed study related to its characterization and triboelectric performance was studied in detail.[8] The silane-based modification on castor oil was previously performed by synthesizing hybrids such as castor oil-amine-TMSPM and castor oil-amine-TMSPM-VTES. The acronyms corresponding to TMSPM and VTES are 3-(trimethoxysilyl) propyl methacrylate (TMSPM) and vinyltriethoxysilane (VTES), respectively. For the preparation of the castor oil-amine-TMSPM hybrid, castor oil and para-aminobenzoic acid were made to react at 100 °C for 8 h in the presence of p-toluenesulfonic acid as a catalyst. Later, TMSPM and boron trifluoride etherate were added to the above mixture, and the reaction was maintained at 50 °C for 24 h. Further, castor oil-amine-TMSPM-VTES was prepared by adding the desired concentration of VTES at 50 °C, and the reaction was continued for 2 h. UV-cured films were formed by mixing these hybrids with a photo-initiator and cross-linker, then casting onto a glass slide using the doctor blade technique.

### *4. Deposition of nanocellulose on graphene-coated PET substrate*

Similar to the agar substrate, an ultrathin triboelectric component (electrode and triboelectric layer) was spray-coated onto a hydrophobic non-degradable PET substrate.

*Graphene deposition on PET substrates*

Prior to deposition, the PET substrate was cleaned with isopropyl alcohol and DI water. With continuous thermal treatment at 60°C, 40 layers of graphene were deposited onto PET to form an ultrathin electrode.

*NC deposition on graphene-coated PET substrate*

Similar to agar, for the fabrication of a dielectric layer onto layered graphene-coated PET substrate, 70 layers of NCs were deposited, wherein thicker layers resulted in delamination due to the development of internal stresses during drying. Therefore, the PET substrate has a multilayer triboelectric component with 40 layers of graphene electrode and 70 layers of NC triboelectric layer named (NC-Gr-PET).

**Figure S1.** Photograph showing a transparent and agar film.

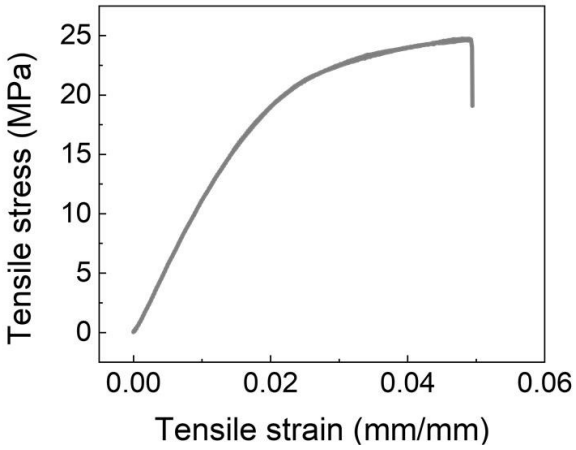


**Figure S2.** Stress-strain curve demonstrating the mechanical stability of the agar substrate film.

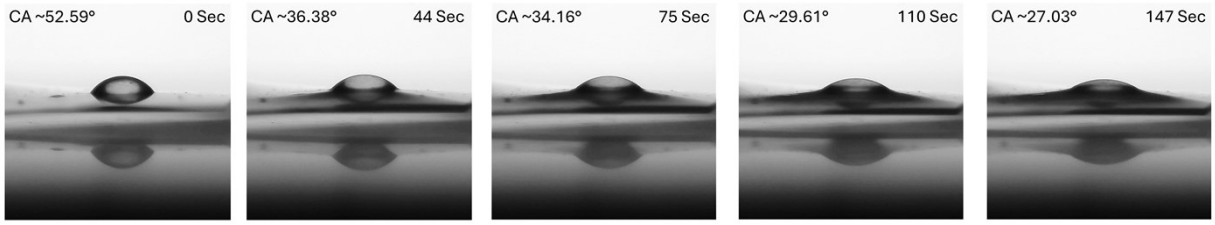


**Figure S3.** Water contact angle on agar, a hygroscopic substrate, and its variation over time due to absorption and spreading.

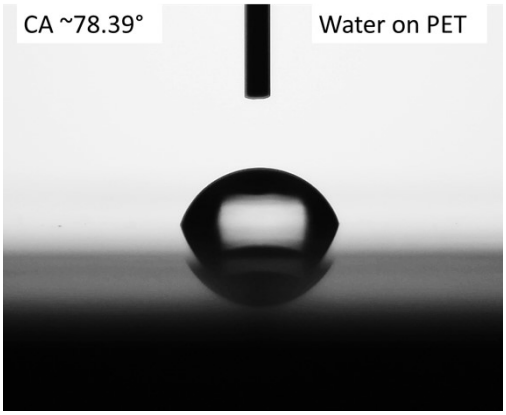


**Figure S4.** Water contact angle on PET which has relatively non-hydrophilic and non-absorbing nature.

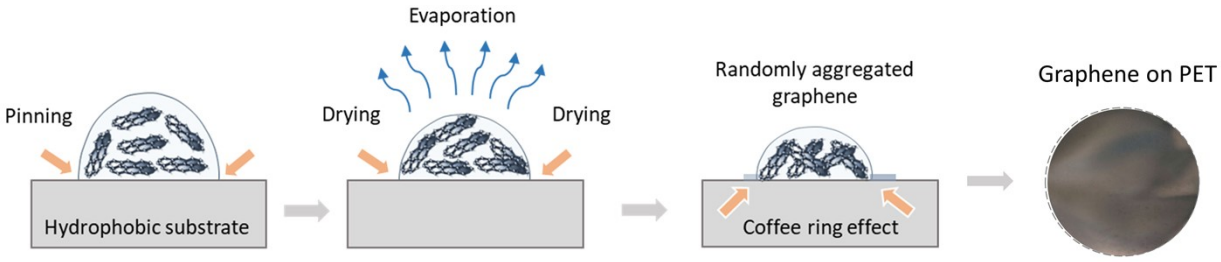


**Figure S5.** Deposition mechanism and photograph of graphene spray-coating on a PET substrate.

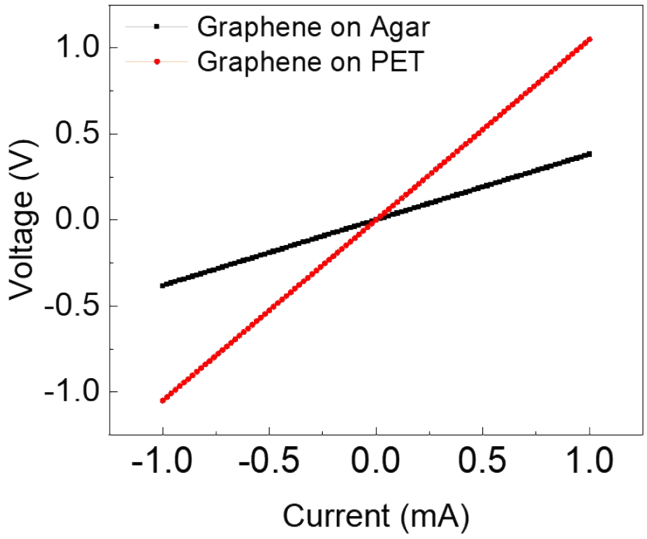


**Figure S6.** Voltage vs. current (IV) curve of graphene on agar and PET obtained using four probe methods.

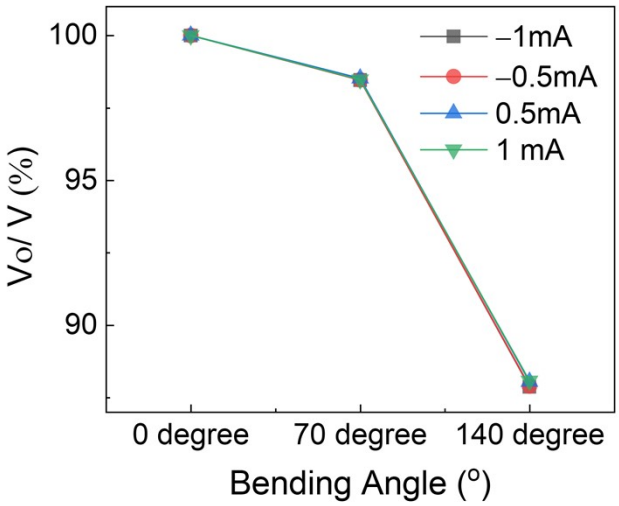


**Figure S7.** The voltage variation ($V_0$/V×100) at different current levels reveals a minimal impact on the electrical conductivity across various bending angles.

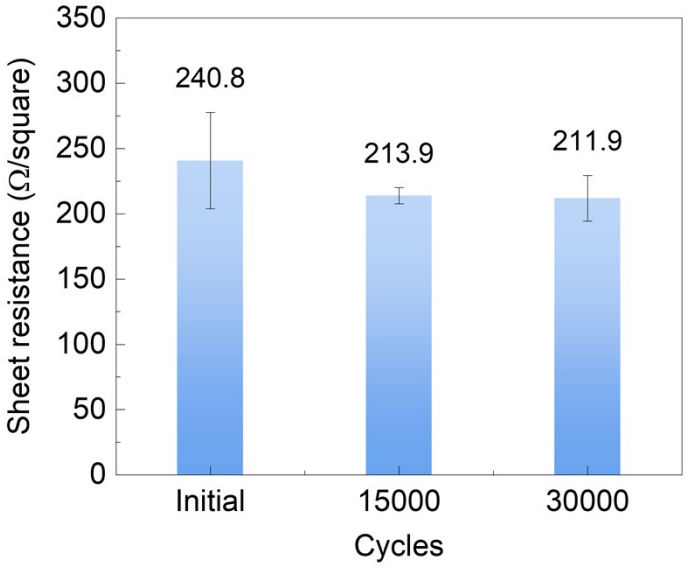


**Figure S8.** Stable sheet resistance of the graphene layer after different bending cycles.

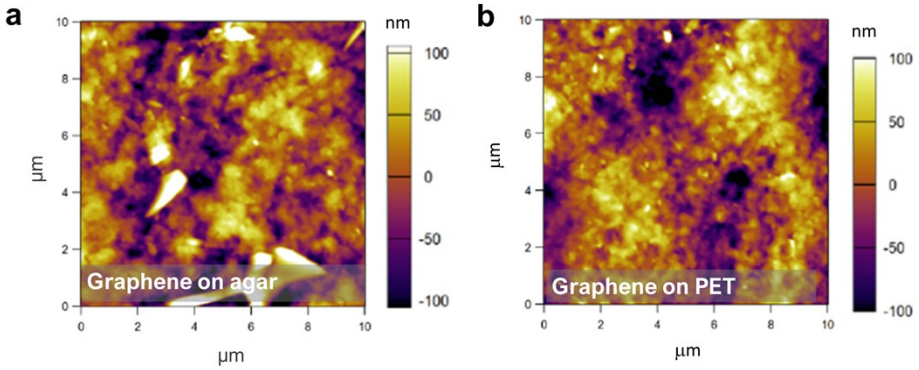


**Figure S9.** AFM image of spray-coated graphene on (a) agar and (b) PET substrate.

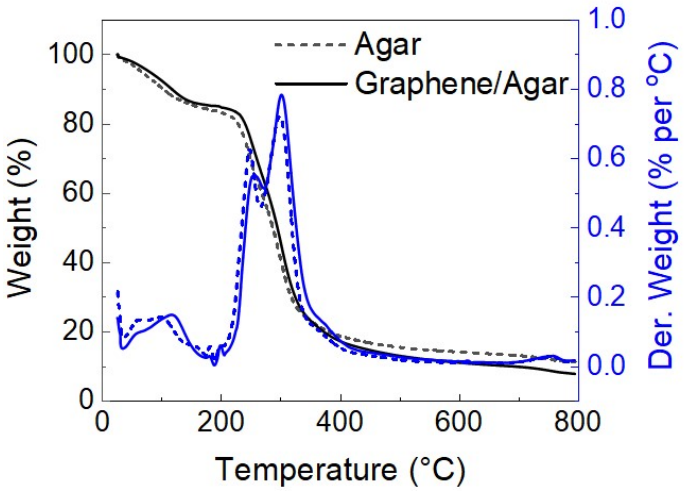


**Figure S10.** TGA and DTG curves for the agar and graphene-coated agar films show the corresponding thermal stability.

**Figure S11**. Photographic image of ultrathin NC and graphene layer on relatively hydrophobic PET substrate.

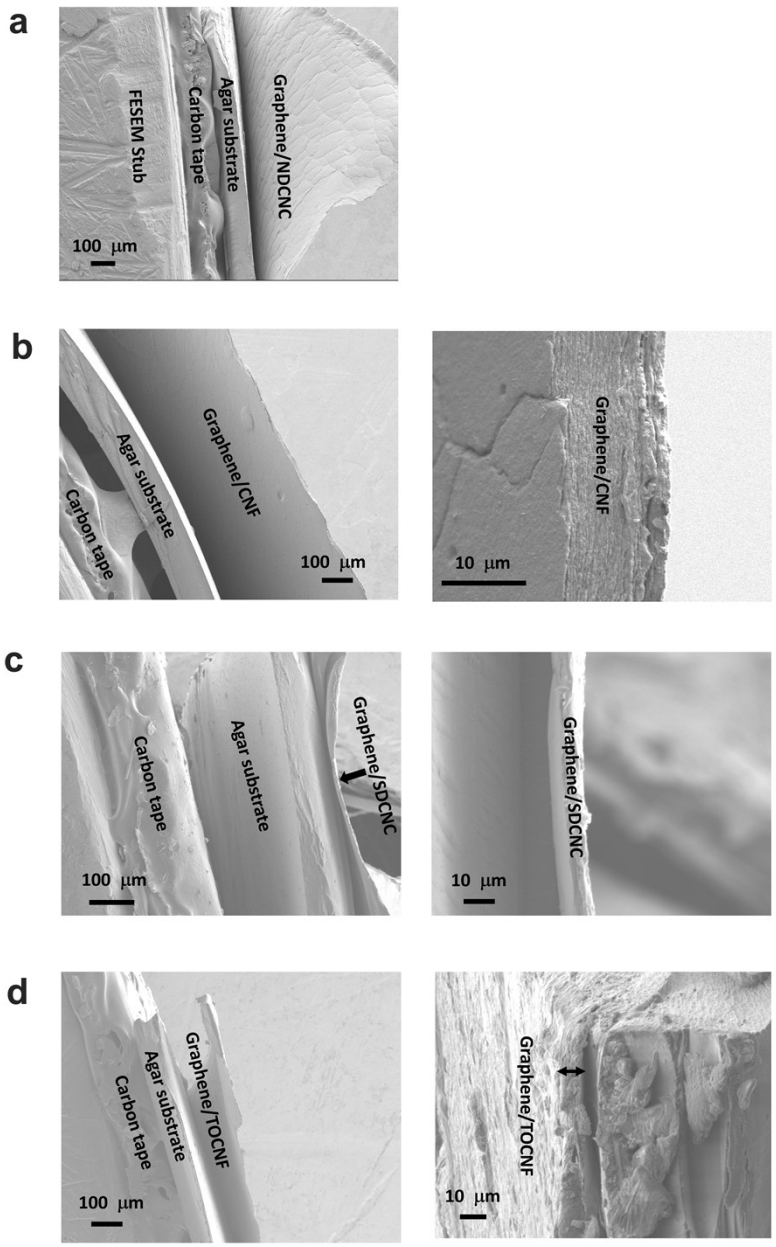


**Figure S12**. FESEM of all NC based NC-Gr-A triboelectric component showing uniform deposition and thickness of active layers (NC/Gr) on agar.

## *5. Free-standing NC(FNC) films and FNC-TENG*

### *5.1. Preparation of free-standing nanocellulose (FNC) film (tribopositive layer)*

To prepare ultrathin FNC film, the desired concentration of all four different types of NC was prepared (1-3 wt%). A smooth, metallic substrate (Cu tape) was chosen to facilitate the easy removal of the sprayed ultrathin film. Initially, the Cu tape was attached to the PET substrate, and the NC suspension was sprayed on top. The surface was fully covered with the sprayed NC droplets in each pass and dried (~ few tens of seconds) before performing the second pass. Each NC film resulted from a total of 80 passes.

### **5.2.** *Preparation of FNC-based TENG (FNC-TENG)*

TENG with an active area of 3×3 $cm^2$ was made by attaching FNC films (NDCNC, SDCNC, CNF, and TOCNF) to the adhesive side of copper tape, and later, PET film-based substrate was attached to the copper tape using thin double-sided tape to form a triboelectric component *(NC/Cu/PET)*. Another device component was prepared by adding commercial polyimide (PI) to the adhesive side of the copper tape while using PET as a substrate (*PI/Cu/PET*). Here, NC films and PI films were used as positive and negative triboelectric layers, respectively. Moreover, all the devices were operated in contact-separation mode, where the contact and separation of the triboelectric layers were done using an automated setup.

### *5.3. FNC film properties*

To assess the inherent properties of the NC dispersions, FNC films were prepared by layer-by-layer spraying onto hydrophobic substrates and then peeled off. **Figure S13a** shows a schematic diagram and a photographic image of a large area of FNC film. **Figure S13b** shows the photographic image of all the resulting free-standing films: CNF, NDCNC, SDCNC, and TOCNF. All the resulting films were transparent and rather smooth, apart from TOCNF, which appeared to

be crumbled, most likely due to its highly crystalline content and mechanical rigidity.[9] **Figure S13c** presents photographs of the free-standing NDCNC film, exhibiting a thickness of approximately 6 μm, which confirms the successful formation of an ultrathin NC layer. Additionally, the same figure demonstrates that the fabricated NC films exhibited remarkable stability in water, both under normal conditions and during bath sonication, despite being ultrathin and binder-free. The photographs also reveal that the films can be shrunk when removed from water and expanded upon re-immersion, maintaining their free-standing nature. Remarkably, these NC films demonstrated resilience to ultrasonication, contrasting with previously reported FNC films prepared via the vacuum filtration technique (data not shown).[10]

### *5.4. FNC-TENG output*

**Figure S13d** shows a schematic of the TENG device architecture prepared using FNC film as a positive triboelectric against a tribonegative PI film, with both tribocomponents using Cu electrode and PET substrate. **Figure S13e** shows the triboelectric performance of the different FNC-TENGs. While no major differences can be observed in the performance, the NDCNC and the CNF based TENGs yielded a higher overall performance with voltage values of ~375 V and ~340 V, respectively. SDCNC and TOCNF show a decreased output of 290 V and 310 V, respectively. The best-performing TENG is obtained for the NDCNC ultrathin film, most likely due to the lower degree of aggregation in the NDCNC precursor solutions and the higher surface potential compared to SDCNC, CNF, and TOCNF. With a maximum output voltage of ~375 V, the demonstrated TENG represents one of the best-performing NDCNC-based TENGs, which is remarkable given the ultrathin nature of the free-standing sprayed film. Furthermore, measuring the voltage output in both forward and reverse modes is crucial to verify that the observed voltage originates solely from the device, without any contributions from external factors. **Figure S13f**

shows the voltage output of the TOCNF-based NC–TENG operated in contact-separation mode, showing a consistent change with the electrode polarity.

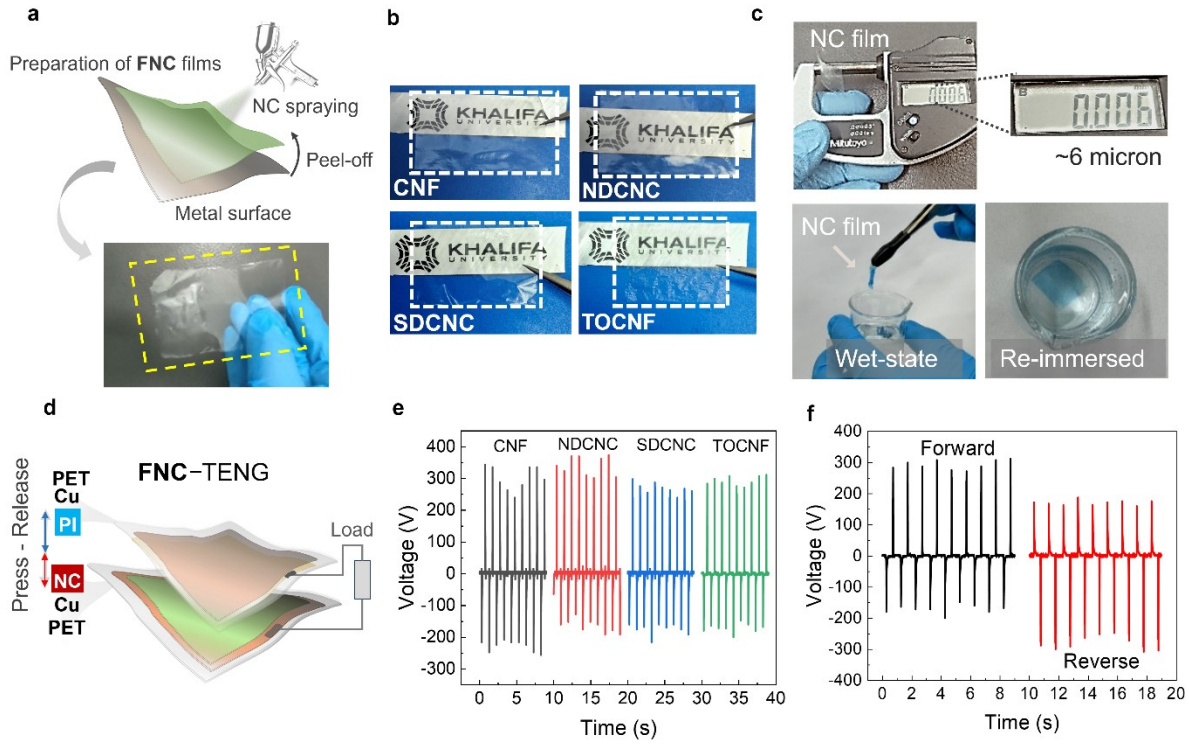


**Figure S13. (a)** Schematically represented layer-by-layer spray coating of NCs on the metallic substrate for the preparation of FNC film, and a photographic image of a large area of FNC film. **(b)** Photographic image of a transparent, layered ultrathin NC film made of CNF, NDCNC, SDCNC, and TOCNF, showing visual differences between the NC films. **(c)** Image showing thickness measurement of the NC film using a digital micrometer, where 6 microns refers to the thickness of ultrathin layered NDCNC film, and photographs showing hydro-responsive shape-memory effect, where the wet NC film is shown to form a folded structure, and the next image shows the unfolding of NC back to its original film form due to interaction with water molecules. **(d)** Schematic illustration of the FNC-TENG prepared using NC films as positive tribo-layers and commercial copper tape as an electrode against a PI negative triboelectric layer. **(e)** Plot showing the voltage output response of the various FNC-TENG made of CNF, NDCNC, SDCNC, and TOCNF. **(f)** Forward and reverse mode voltage output of TOCNF-based FNC-TENG.

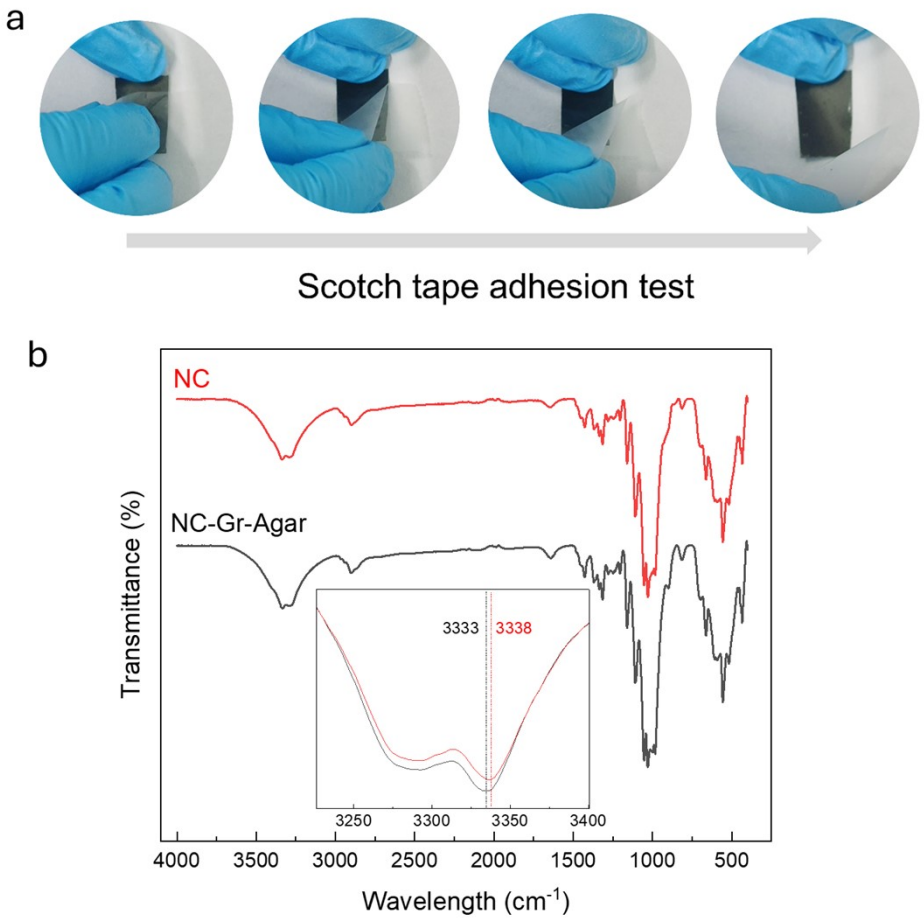


**Figure S14.** Characterization of interfacial strength between layers. **(a)** Images showing different stages of the tape test to evaluate the interfacial strength between ultrathin layers of NC/graphene and graphene/agar. **(b)** FTIR spectra of NC and NC-Gr-A layers made of NDCNC.

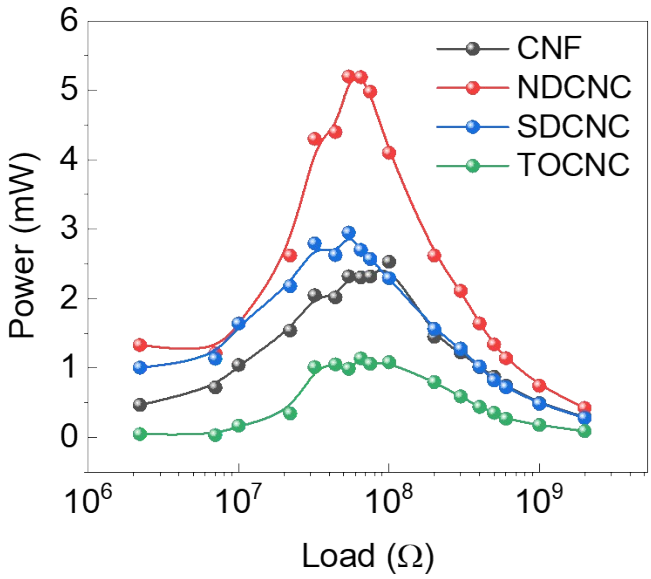


**Figure S15.** Power output of *NC–Gr–A* TENGs made of CNF, NDCNC, SDCNC and TOCNC with varying load resistance values ranging from 2 MΩ to 2 GΩ.

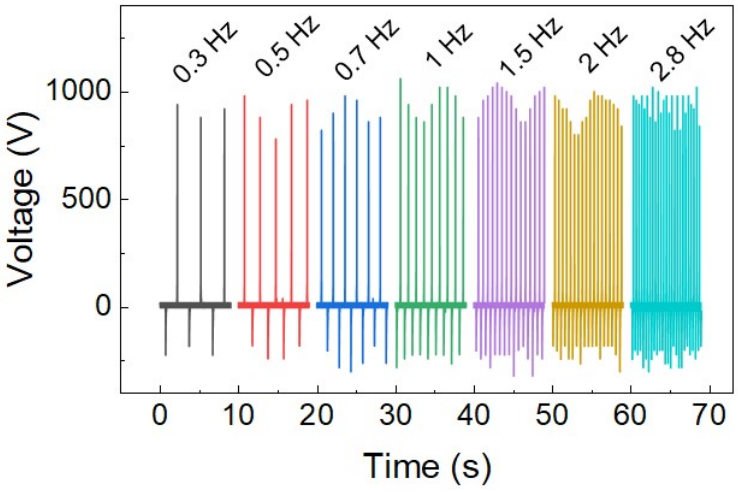


**Figure S16.** Frequency-dependent voltage output for the best-performing NDCNC-based *NC–Gr–A* TENG.

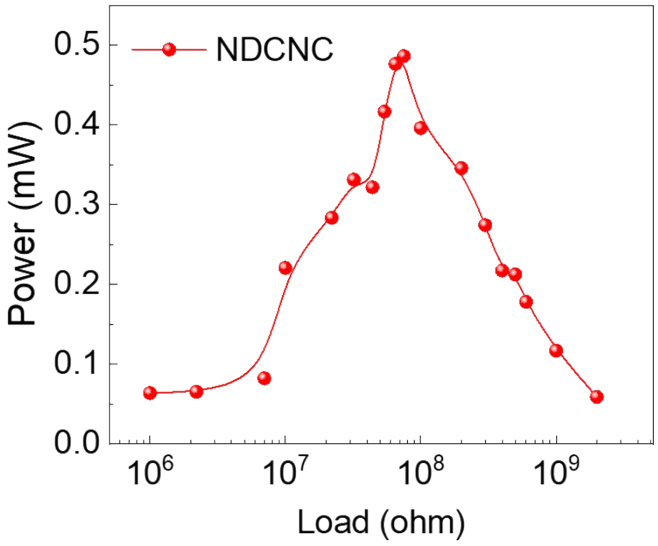


**Figure S17.** The power output of the best-performing bio-TENG, made of an NDCNC and CO pair as triboelectric layers, with varying load resistance values ranging from 1 MΩ to 2 GΩ.

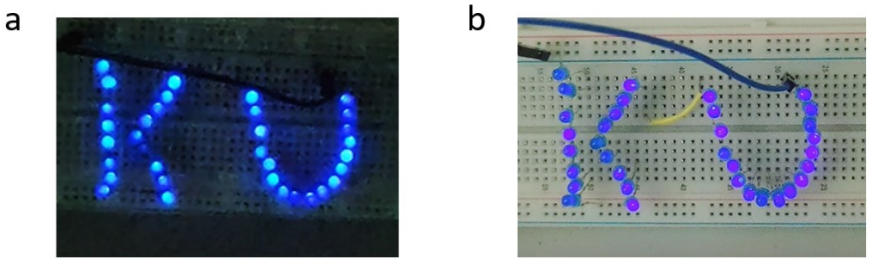


**Figure S18.** Lighting up multiple LEDs connected in series using bio-TENG made of NDCNC and CO as triboelectric layers.

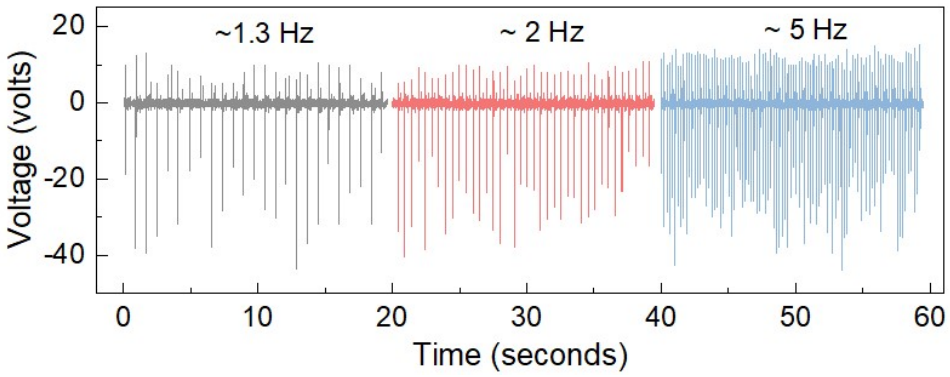


**Figure S19.** Frequency-dependent voltage output of ZG−TENG.

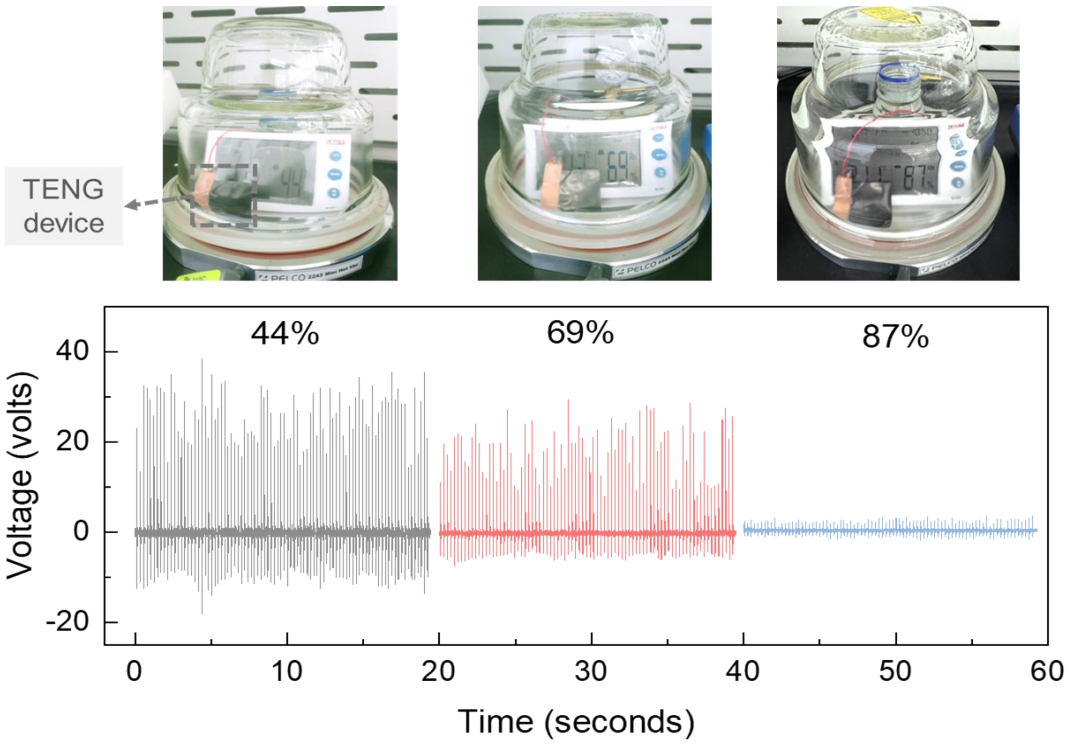


**Figure S20.** Humidity-dependent voltage response of ZG−TENG.

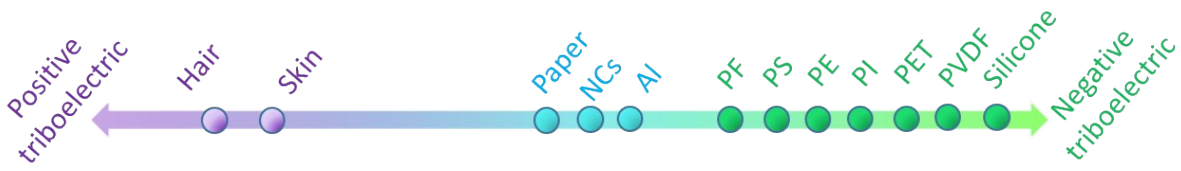


**Figure S21.** Triboelectric series based on the output voltage of *NC–Gr–A* based All-PS SE-TENG when NDCNC is made to contact relatively positive, neutral and negative triboelectric materials, namely as hair, skin aluminum, paper, polystyrene (PS), polyethylene (PE), polyimide (PI), polyvinylidene fluoride (PVDF) and silicone.

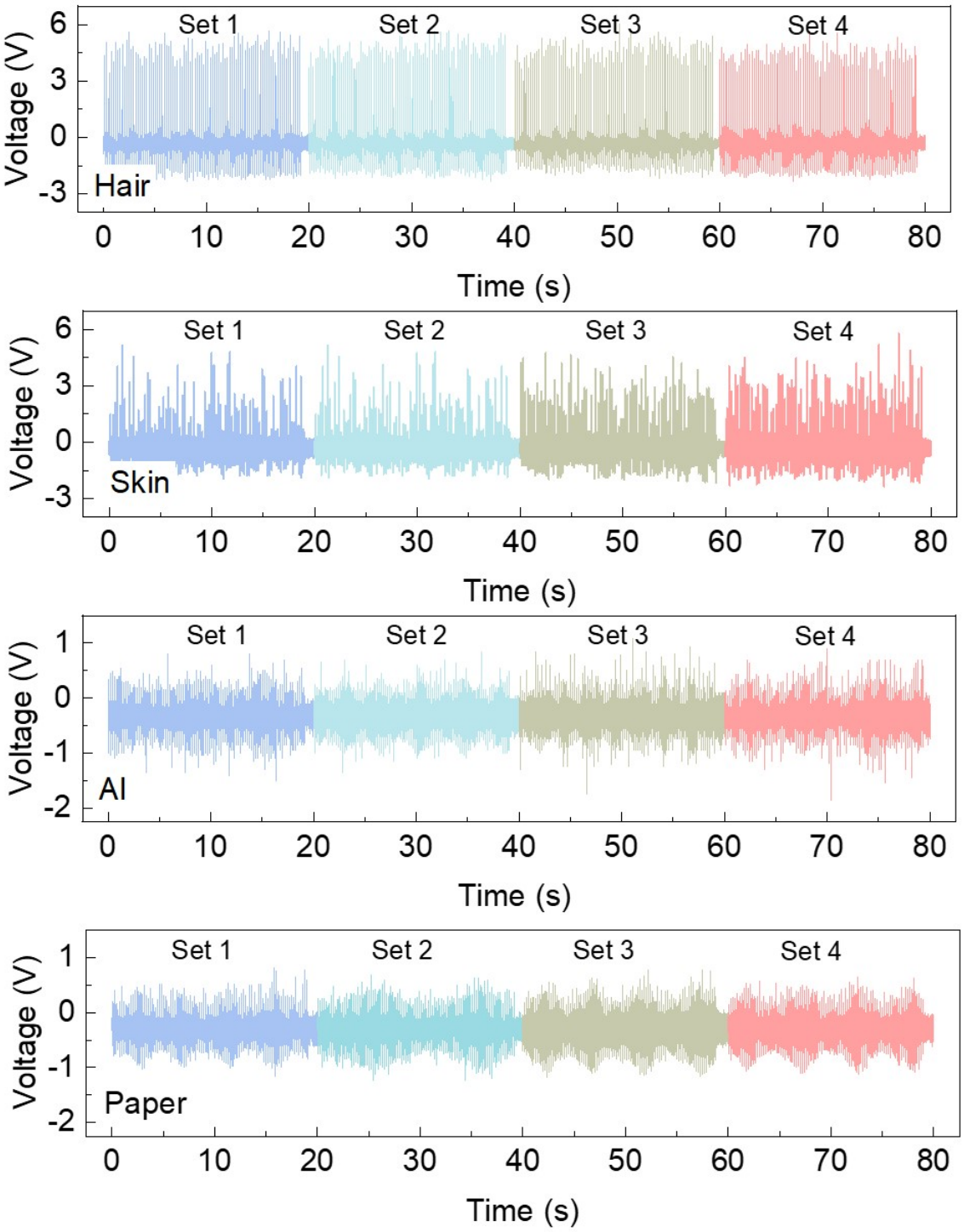


**Figure S22**. Voltage output of All-PS SE-TENG for all the tribopositive materials: hair, skin, aluminum, and paper for four sets (400 cycles).

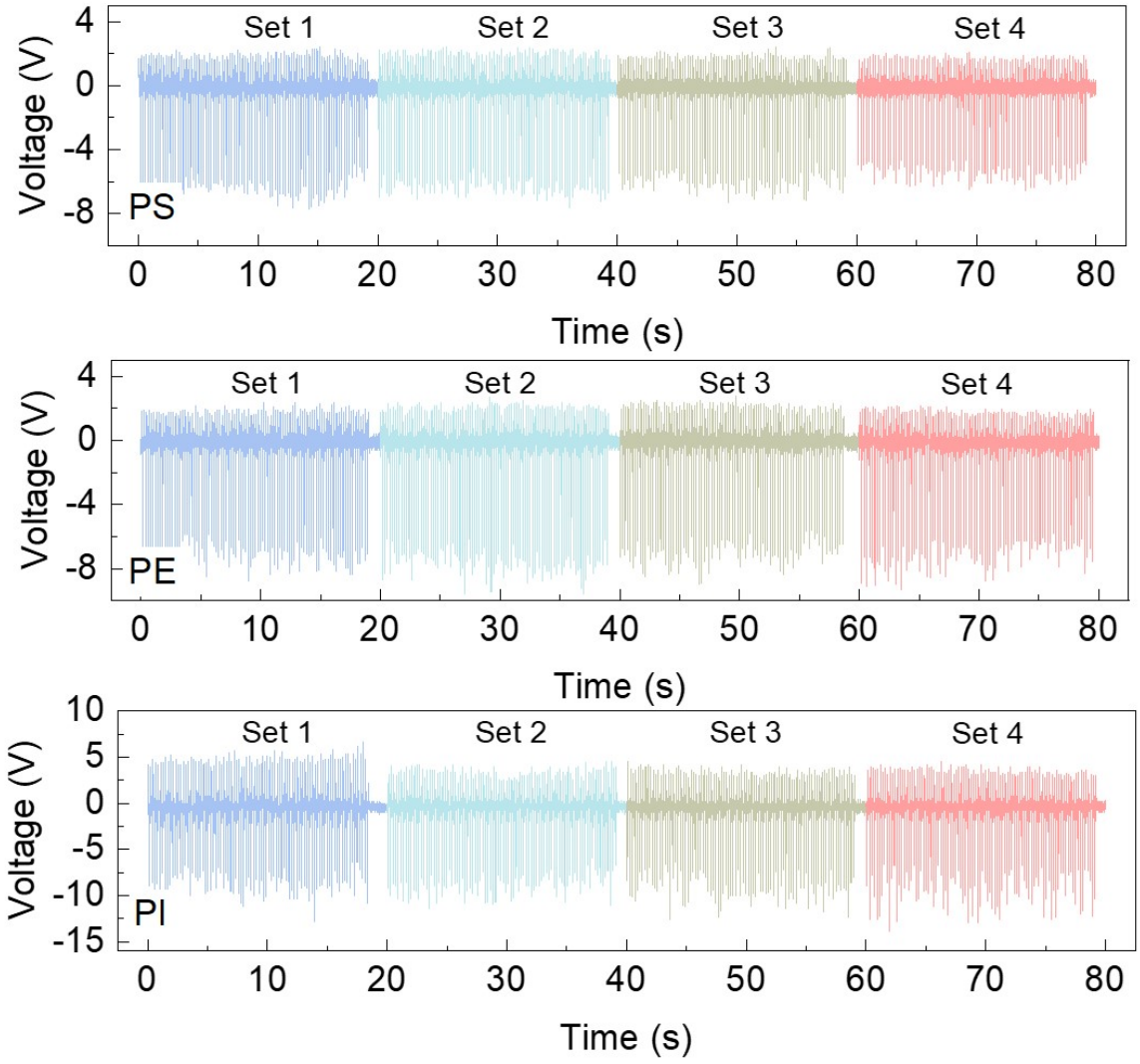


**Figure S23.** Consistent voltage output and polarity of SE−TENG when sensing was done for slightly tribonegative material with respect to NC: PS, PE and PI.

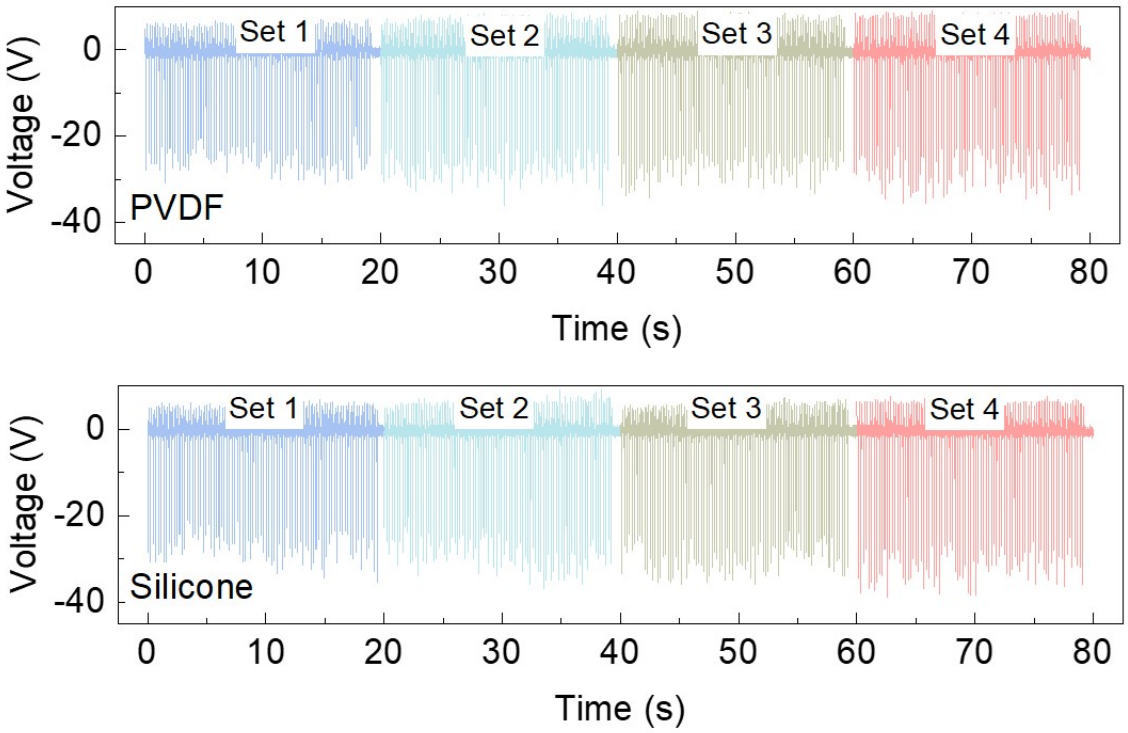


**Figure S24.** Voltage output of SE-TENG for highly tribonegative materials: PVDF and silicone, for all four sets.

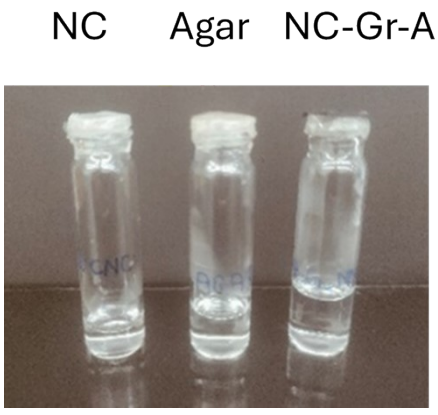


**Figure S25.** Photograph showing different levels of water after 20 days for NC, agar and NC-Gr-A layer, aligning well with the moisture permeability data.

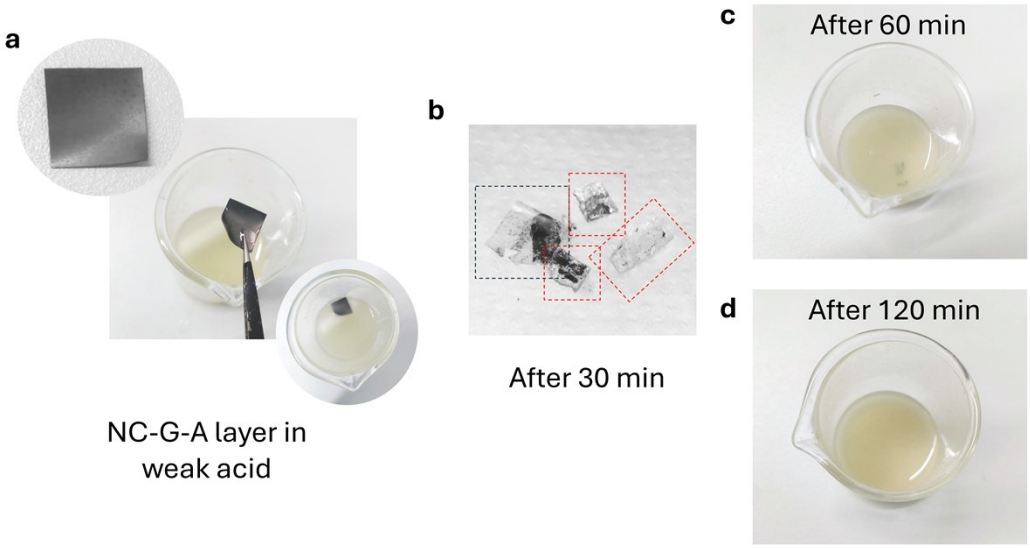


**Figure S26.** Degradation of NC-Gr-A layer in weak naturally extracted acidic solution.

**Table S1.** Comparison of our devices with other cellulose-based devices reported in the literature.

| S. No | Tribo-electric Material | Nature of triboelectric layers | Electrode Material | Thickness of triboelectric layer (μm) | Thickness of electrode (μm) | Mode of Opera-tion | Output Voltage (Volts)/ power density (mW/m²) | Application | | | Ref. |
|---|---|---|---|---|---|---|---|---|---|---|---|
| | | | | | | | | Type | Output Voltage (Volts) | Properties | |
| **Cellulose-based TENGs** | | | | | | | | | | | |
| 1. | CNC/MC, PTFE | Biopolymer vs synthetic polymer | Al/ graphite | 20 | 20/~65 | CS | ~200/ 1000 | Respiration monitoring | 0.8 | Degradable in water/ soil | **[11]** |
| 2. | BC, Cu | Biopolymer vs synthetic polymer | Cu | ---/~65 | ~65 | CS | ~13/4.4 | --- | --- | --- | **[12]** |
| 3. | CNF, FEP | Biopolymer vs synthetic polymer | ITO | ~70-320/60 | Nm | CS | ~30/ ~6mW | Biomechanical energy harvesting | ~30 | --- | **[13]** |
| 4. | Paper, FEP (Hybrid) | Biopolymer vs synthetic polymer | ITO | ~120/25 | nm | CS/ SE | ~90/ ~300 | Wireless human machine interaction system | ~25 | --- | **[14]** |
| 5. | Egg white, chitin, cellulose, raw silk, rice paper | All-biopolymer | Mg | 100 | nm | CS | ~50 | Biodegradable Implants | ~ 5 | --- | **[15]** |
| 6. | Cellulose, Cellulose +Ag | All-biopolymer (including substrate) | Ag nanowire | --- | --- | CS | ~21/693 | Writable surface | --- | Green device | **[10]** |
| 7. | BC+$BaTiO_3$, PDMS | Biopolymer vs synthetic polymer | Cu | 50/100 | ~65 | CS | ~181/ 4800 | Biomechanical energy harvesting | ~15-40 | --- | **[16]** |
| 8. | 3D printed PDMS, CNF aerogel | Biopolymer vs synthetic polymer | Ag | mm | --- | CS | ~50 | Biomechanical motion sensor, humidity responder | ~6 | All printed devices | **[17]** |
| 9. | CNF, FEP | Biopolymer vs synthetic polymer | Cu | --- | --- | CS | ~76/ --- | --- | --- | --- | **[18]** |
| 10. | Cellulose /skin, PDMS | Biopolymer vs synthetic polymer | PP coated fabric | mm | Mm | CS | ~200/ 900 | Powering portable electronics | --- | --- | **[19]** |
| 11. | Paper, PVC, PET | Biopolymer vs synthetic polymer | Paper+ Ag nanowire | A few hundreds of microns | Nm | FS | ~100 | Soft tissue paper | --- | Ultrasoft, cuttable, green | **[20]** |
| 12. | PCL+GO, cellulose | All-biopolymer (including substrate) | Au | 50-200/83 | Nm | CS | ~120/ 72.5 | --- | --- | --- | **[21]** |
| 13. | PLGA, PHB/V, PVA, PCL | All-biopolymer | Mg | 100(PHBV)/ 50-100 (PCL) | | CS | 40/32.6 | Biodegradable implants | | Biocompatible | **[22]** |
| 14. | BC, PPBC,PDBC, SBC, PVDF | Biopolymer vs synthetic polymer | Cu | 25-85 (BCs)/ ~30 (PVDF) | ~65 | CS | ~1010/ 8700 | Powering scientific calculator | --- | --- | **[23]** |

| | | | | | | | | | | | |
|---|---|---|---|---|---|---|---|---|---|---|---|
| | BC, PPBC, PDBC, SBC | All-biopolymer | Cu | 25-85 | ~65 | CS | ~42.7/9.2 | Powering portable electronics | --- | Biocompatible | |
| | PDBC | All-biopolymer (including substrate) | MWCNT/BC | 39 | 48 | SE | ~200 | Wearable, conformable biomechanical energy harvester | ~43 | Breathable, degradable antibacterial, | |
| 15. | CO/PI | Biopolymer vs synthetic polymer | Cu, Al | 30-50 | ~65 | CS | ~330/450 | --- | --- | Highly tribo-negative bio-polymer | **[24]** |
| | CO/CO-VT-5 | All-biopolymer | Cu, Al | 30-50 | ~65 | CS | ~55/18 | --- | --- | Highly tribo-negative bio-polymer | |
| | CO-VT-5 | All-biopolymer | Al | 30-50 | ~65 | SE | ~75 | --- | --- | Highly tribo-negative bio-polymer | |
| **Ultrathin TENGs** | | | | | | | | | | | |
| 16. | NC | Biopolymer vs synthetic polymer (PET substrate) | graphene | 13-181 nm | 200 nm | SE | | Biomechanical energy harvesting (piano playing) | 1.4 V capacitor charging (1 min) | Ultrathin structure | **[25]** |
| 17. | NC/PI | Biopolymer vs synthetic polymer | Cu | 6/30 | ~65 | CS | ~375 | --- | --- | Ultrathin tribolayer | **This work** |
| | NC/PI | Biopolymer vs synthetic polymer | Graphene/ Cu | 6/30 | 4/~65 | CS | ~1070/5.76 W/m$^2$ | --- | --- | Ultrathin positive tribolayer/ electrode | |
| | NC/CO | All-biopolymer | Graphene/ Al | 6/50 | 4/~65 | CS | ~300/0.54 Wm$^2$ | Powering portable electronics | --- | Ultrathin positive tribolayer/ electrode | |
| | NC | All-biopolymer (including substrate) | Graphene | 6 | 4 | SE | ~60 | Material sensing, biomechanical energy harvester, powering portable electronics | --- | Skin like all-biopolymeric structure | |

## Reference


[1] K.W. Klockars, B.L. Tardy, M. Borghei, A. Tripathi, L.G. Greca, O.J. Rojas, Effect of anisotropy of cellulose nanocrystal suspensions on stratification, domain structure formation, and structural colors, Biomacromolecules, 19 (2018) 2931-2943.
[2] B.L. Tardy, B.D. Mattos, L.G. Greca, T. Kämäräinen, K.W. Klockars, O.J. Rojas, Tessellation of chiral-nematic cellulose nanocrystal films by microtemplating, Advanced Functional Materials, 29 (2019) 1808518.
[3] B.D. Mattos, B.L. Tardy, L.G. Greca, T. Kämäräinen, W. Xiang, O. Cusola, W.L.E. Magalhães, O.J. Rojas, Nanofibrillar networks enable universal assembly of superstructured particle constructs, Science Advances, 6 eaaz7328.
[4] B.D. Mattos, B.L. Tardy, O.J. Rojas, Accounting for substrate interactions in the measurement of the dimensions of cellulose nanofibrils, Biomacromolecules, 20 (2019) 2657-2665.
[5] M.S. Reid, M. Villalobos, E.D. Cranston, Benchmarking cellulose nanocrystals: From the laboratory to industrial production, Langmuir, 33 (2017) 1583-1598.
[6] O.I.V. Luotonen, L.G. Greca, G. Nyström, J. Guo, J.J. Richardson, O.J. Rojas, B.L. Tardy, Benchmarking supramolecular adhesive behavior of nanocelluloses, cellulose derivatives and proteins, Carbohydrate polymers, 292 (2022) 119681.
[7] M. Beaumont, B.L. Tardy, G. Reyes, T.V. Koso, E. Schaubmayr, P. Jusner, A.W.T. King, R.R. Dagastine, A. Potthast, O.J. Rojas, T. Rosenau, Assembling native elementary cellulose nanofibrils via a reversible and regioselective surface functionalization, Journal of the American Chemical Society, 143 (2021) 17040-17046.
[8] K.K. Jena, B. Fatma, S.S. Arya, S.M. Alhassan, V. Chan, A.M. Pappa, C. Pitsalidis, High performance flexible triboelectric nanogenerators using bio-derived films made of siloxane-modified castor oil, Journal of Materials Chemistry A, (2024).
[9] K.W. Klockars, L.G. Greca, J. Majoinen, K. Mihhels, O.J. Rojas, B.L. Tardy, Drying stresses in cellulose nanocrystal coatings: Impact of molecular and macromolecular additives, Carbohydrate polymers, 303 (2023) 120465.
[10] I. Kim, H. Jeon, D. Kim, J. You, D. Kim, All-in-one cellulose-based triboelectric nanogenerator for electronic paper using simple filtration process, Nano Energy, 53 (2018) 975-981.
[11] T. Wang, S. Li, X. Tao, Q. Yan, X. Wang, Y. Chen, F. Huang, H. Li, X. Chen, Z. Bian, Fully biodegradable water-soluble triboelectric nanogenerator for human physiological monitoring, Nano Energy, 93 (2022) 106787.
[12] H.-J. Kim, E.-C. Yim, J.-H. Kim, S.-J. Kim, J.-Y. Park, I.-K. Oh, Bacterial nano-cellulose triboelectric nanogenerator, Nano Energy, 33 (2017) 130-137.
[13] C. Yao, A. Hernandez, Y. Yu, Z. Cai, X. Wang, Triboelectric nanogenerators and power-boards from cellulose nanofibrils and recycled materials, Nano Energy, 30 (2016) 103-108.
[14] X. He, Y. Zi, H. Yu, S.L. Zhang, J. Wang, W. Ding, H. Zou, W. Zhang, C. Lu, Z.L. Wang, An ultrathin paper-based self-powered system for portable electronics and wireless human-machine interaction, Nano Energy, 39 (2017) 328-336.
[15] W. Jiang, H. Li, Z. Liu, Z. Li, J. Tian, B. Shi, Y. Zou, H. Ouyang, C. Zhao, L. Zhao, R. Sun, H. Zheng, Y. Fan, Z.L. Wang, Z. Li, Fully bioabsorbable natural-materials-based triboelectric nanogenerators, Advanced Materials, 30 (2018) 1801895.
[16] Y. Shao, C.-p. Feng, B.-w. Deng, B. Yin, M.-b. Yang, Facile method to enhance output performance of bacterial cellulose nanofiber based triboelectric nanogenerator by controlling micro-nano structure and dielectric constant, Nano Energy, 62 (2019) 620-627.
[17] C. Qian, L. Li, M. Gao, H. Yang, Z. Cai, B. Chen, Z. Xiang, Z. Zhang, Y. Song, All-printed 3d hierarchically structured cellulose aerogel based triboelectric nanogenerator for multi-functional sensors, Nano Energy, 63 (2019) 103885.

[18] Y. Liu, Q. Fu, J. Mo, Y. Lu, C. Cai, B. Luo, S. Nie, Chemically tailored molecular surface modification of cellulose nanofibrils for manipulating the charge density of triboelectric nanogenerators, Nano Energy, 89 (2021) 106369.
[19] A.R. Mule, B. Dudem, H. Patnam, S.A. Graham, J.S. Yu, Wearable single-electrode-mode triboelectric nanogenerator via conductive polymer-coated textiles for self-power electronics, ACS Sustainable Chemistry & Engineering, 7 (2019) 16450-16458.
[20] C. Wu, T.W. Kima, S. Sung, J.H. Park, F. Li, Ultrasoft and cuttable paper-based triboelectric nanogenerators for mechanical energy harvesting, Nano Energy, 44 (2018) 279-287.
[21] S. Parandeh, M. Kharaziha, F. Karimzadeh, An eco-friendly triboelectric hybrid nanogenerators based on graphene oxide incorporated polycaprolactone fibers and cellulose paper, Nano Energy, 59 (2019) 412-421.
[22] Q. Zheng, Y. Zou, Y. Zhang, Z. Liu, B. Shi, X. Wang, Y. Jin, H. Ouyang, Z. Li, Z.L. Wang, Biodegradable triboelectric nanogenerator as a life-time designed implantable power source, Science Advances, 2 e1501478.
[23] B. Fatma, S.M. Andrabi, S. Gupta, V. Verma, A. Kumar, C. Pitsalidis, A. Garg, Biocompatible, breathable and degradable microbial cellulose based triboelectric nanogenerator for wearable transient electronics, Nano Energy, 114 (2023) 108628.
[24] K.K. Jena, B. Fatma, S.S. Arya, S.M. Alhassan, V. Chan, A.M. Pappa, C. Pitsalidis, High performance flexible triboelectric nanogenerators using bio-derived films made of siloxane-modified castor oil, Journal of Materials Chemistry A, 12 (2024) 8340-8349.
[25] M.S. Alghamdi, J.J. Morgan, K. Walsh, D.W. Shin, R. Nigmatullin, Z. Saadi, J. Routledge, A.I.S. Neves, S. Russo, S.J. Eichhorn, M.F. Craciun, Triboelectric nanogenerator based on cellulose nanocrystals and graphene for energy harvesting from piano playing motion, Nano Energy, 138 (2025) 110816.